Altered Huntingtin-Chromatin Interactions Predict Transcriptional and Epigenetic Changes in Huntington's Disease

Jocelynn R Pearl* (1,2), Amol C Shetty* (3), Jeffrey P Cantle (5), Dani E Bergey (1), Robert M. Bragg (5), Sydney R. Coffey (5), Holly B. Kordasiewicz (4), Leroy E Hood (1), Nathan D Price (1), Seth A Ament (3) **, Jeffrey B Carroll (5) **

1. Institute for Systems Biology, Seattle, Washington
2. Molecular & Cellular Biology Graduate Program, University of Washington, Seattle, Washington
3. Institute for Genome Sciences, University of Maryland School of Medicine, Baltimore, MD
4. Ionis Pharmaceuticals, Carlsbad, CA
5. Behavioral Neuroscience Program, Department of Psychology, Western Washington University, Bellingham, Washington

*co-first authors

**co-corresponding authors: jeff.carroll@wwu.edu / SAment@som.umaryland.edu

Summary

Progressive striatal gene expression changes and epigenetic alterations are a prominent feature of Huntington's disease (HD), but direct relationships between the huntingtin (HTT) protein and chromatin remain poorly described. Here, using chromatin immunoprecipitation and sequencing (ChIP-seq), we show that HTT reproducibly occupies specific locations in the mouse genome, including thousands of genomic loci that are differentially occupied in striatal tissue from a knock-in mouse model of HD (B6.*Htt*$^{Q111/+}$) versus wildtype controls. ChIP-seq of histone modifications, generated in parallel, revealed genotype-specific colocalization of HTT with trimethylation of histone 3 lysine 27 (H3K27me3), a repressive chromatin mark. Near genes that are differentially regulated in HD, greater HTT occupancy in *Htt*$^{Q111/+}$ vs. wildtype mice predicted increased H3K27me3, reduced histone 3 lysine 4 (H3K4me3), a marker of poised and active promoters, and down-regulated gene expression. Altered huntingtin-chromatin interactions may therefore play a direct role in driving transcriptional dysregulation in HD.

Introduction

Huntington's disease (HD) is a fatal dominant neurodegenerative disease caused by expansion of a glutamine-coding (polyQ) CAG tract near the 5' end of the *Huntingtin* (*HTT*) gene (MacDonald et al., 1993). Clinical symptoms include deficits in motor control and cognition, as well as psychiatric symptoms. HD progression is linked to the selective death of medium spiny neurons (MSNs) in the striatum (von Schimmelmann et al., 2016). In the cell, HTT protein dynamically shuttles between the cytoplasm and nucleus, where it plays functionally important but poorly understood roles. Mis-localization of mutant HTT (mHTT) protein to the nucleus and transcriptional (Cha, 2007); (Langfelder et al., 2016) and epigenomic (Bassi et al., 2017); (Achour et al., 2015); (Le Gras et al., 2017) dysregulation are among the earliest phenotypes in cells and tissues expressing mHTT and are highly reproducible in brain tissue from human HD (Ament et al., 2018; Hodges et al., 2006). However, while it is clear that mHTT expression in the nucleus is sufficient to drive transcriptional dysregulation, the molecular mechanisms by which mHTT mediates this are poorly understood. Characterizing and potentially preventing or reversing these mechanisms could have clinical relevance, as mis-localization of mutant HTT (mHTT) to the nucleus is a critical driver of mHTT-mediated neuronal death, both *in vitro* (Saudou et al., 1998) and in mouse models of the HD mutation (Gu et al., 2015).

A straightforward hypothesis is that HTT and/or mHTT directly contribute to transcriptional dysregulation in HD by occupying specific locations on chromatin DNA. To date, interactions of HTT with chromatin remain obscure, but they are supported by several lines of indirect evidence: (i) chromatin immunoprecipitation indicates that HTT affiliates with chromatin DNA (Benn et al., 2008); (ii) the HTT protein contains a series of HEAT domains, which are capable of serving as DNA binding domains (Neuwald, 2000); (iii) HTT forms direct protein-protein interactions with a variety of transcriptional regulatory proteins in the

nucleus, including transcription factors (TFs) and chromatin remodeling factors (Saudou and Humbert, 2016). Perhaps the best understood such interactions involve chromatin remodeling complexes that mediate gene repression and heterochromatin formation. HTT binds in a polyQ-length sensitive manner to Polycomb Repressive Complex 2 (PRC2), the chromatin remodeling complex responsible for trimethylation of lysine 27 on the histone 3 tail (H3K27me3), a critical repressive mark(Seong et al., 2010). Ablation of PRC2 in MSNs reproduces several of the cellular phenotypes in HD, including aberrant de-repression of transcripts that code for developmentally regulated transcription factors, loss of MSN identity gene expression, and prolonged cell death (von Schimmelmann et al., 2016).

To investigate the hypothesis above, we performed chromatin immunoprecipitation and deep sequencing (ChIP-seq) to map HTT genomic occupancy in striatal tissue from the *Htt*$^{Q111/+}$ knock-in mouse model of the HD mutation and in wildtype *Htt*$^{+/+}$ controls. We analyzed these data together with ChIP-seq of the histone modifications H3K27me3 and H3K4me3, the PRC2 effector EZH2, and RNA polymerase II, generated in parallel from tissue-, age- and genotype-matched mice, as well as published RNA-seq data from the striatum of *Htt*$^{Q111/+}$ mice at similar timepoints. We describe thousands of reproducible HTT ChIP-seq peaks, both in *Htt*$^{+/+}$ and *Htt*$^{Q111/+}$ mice, and observe robust genotype-specific patterns of binding, which are correlated with epigenomic and transcriptional changes seen in HD. These results provide, for the first time, a genome-wide map of HTT genomic occupancy and suggest that altered transcription in HD arises, in part, via alterations in direct HTT-chromatin binding.

Results

HTT reproducibly occupies thousands of locations in the mouse genome

We set out to map the genomic occupancy of HTT and its relationship to HD mutations. Chromatin immunoprecipitation and deep sequencing (ChIP-seq) was performed using striatal tissue from four-month-old *Htt*$^{Q111/+}$ and wildtype mice, using a well-validated antibody, EPR5526 (Schut et al., 2015), which recognizes an N-terminal epitope of the HTT protein with no known differences in affinity for wildtype vs. mutant HTT isoforms. We sequenced four biological replicates from *Htt*$^{Q111/+}$ mice and three from *Htt*$^{+/+}$ mice, with each biological replicate consisting of pooled striata from three mice. *Htt*^{Q111} is a well-characterized, genetically precise knock-in mouse model of a mutation associated with juvenile-onset HD, in which a human allele of *Htt* exon 1 with 111 poly-Q encoding CAG repeats has been inserted into the endogenous *Htt* locus. *Htt*$^{Q111/+}$ mice are otherwise isogenic with *Htt*$^{+/+}$ littermate controls. Four-months of age represents an early timepoint in the progression of disease-related phenotypes in *Htt*$^{Q111/+}$ mice. At this age, we (Ament et al., 2017; Bragg et al., 2017) and others (Langfelder et al., 2016) have detected hundreds of differentially expressed genes in striatal tissue and misfolded HTT isoforms in the nuclei of many striatal MSNs, but there is not yet any discernible striatal cell death or glial proliferation (Bragg et al., 2017).

We computed HTT ChIP-seq peaks separately in each sample using MACS2 (Zhang et al., 2008). We detected 10,567 highly reproducible peaks, identified independently at a False Discovery Rate [FDR] < 0.01 in at least 3 biological replicates from *Htt*$^{Q111/+}$ mice and/or in all three replicates from wildtype mice, excluding 'blacklisted' regions empirically determined by the ENCODE project to have a high rate of false positive signals (Table S1; (ENCODE Project Consortium, 2012). Two control experiments supported the reproducibility and biological relevance of these locations of HTT genomic occupancy. First, ChIP-seq (n = 1) using a second HTT antibody, MAB2166 (Trottier et al., 1995), revealed peaks with a high degree of overlap to EPR5526 peaks (Table S2; $\log_2$(FC) = 6.0, p < 1 in 100,000 by permutation, using the Genomic Annotation Tester, GAT; (Heger et al., 2013). Second, we treated *Htt*$^{Q111/+}$ and *Htt*$^{+/+}$ mice with an antisense oligonucleotide (ASO) that reduced HTT levels by an average of 53% in the cortex and performed ChIP-seq (Table S3; Fig. S1A-B, n = 1 per treatment, per genotype) to establish the relationship between HTT protein levels and HTT occupancy. This experiment revealed 10,258 HTT peaks that were reproducible at FDR < 0.01 in at least two of the four samples from mouse cortex. Despite the small sample size and partial HTT knockdown, we detected a global depletion of HTT occupancy in the cortex of mice treated with HTT-lowering ASOs. In ASO-treated mice, occupancy at 4,196 peaks (41%) was >1.5-fold reduced, whereas occupancy at only 1,890 peaks (19%) increased by a comparable amount (more peaks with reduced than increased occupancy: binomial test, p = 5.6e-197; Fig. S1C). >80% of peaks that were significantly differentially occupied between ASO treatment groups (p < 0.05) had decreased occupancy (418 peaks with decreased occupancy vs. 93 peaks with increased occupancy). These results suggest that many of the reproducible peaks identified by HTT ChIP-seq accurately reflect HTT occupancy rather than non-specific signals.

Of the 10,567 highly reproducible peaks in striatum, 6,702 were reproducible uniquely in *Htt*$^{+/+}$ samples (henceforth, "WT-specific"), 1,976 were reproducible uniquely in *Htt*$^{Q111/+}$ samples ("Q111-specific"), and 1,889 were reproducibly identified in both genotypes ("Shared"; Fig. 1B, Table S1). A second approach, quantitative differential binding analysis with edgeR (Robinson et al., 2010), confirmed that the majority of peaks classified as WT-specific and Q111-specific were differentially occupied and were more deeply occupied in *Htt*$^{+/+}$ samples and in *Htt*$^{Q111/+}$ samples, respectively (Fig. 1C-E; Table S1). Interestingly, many peaks classified as Shared were also differentially occupied, with most of these peaks more deeply occupied in *Htt*$^{+/+}$ mice (Fig. 1E). The heterozygous mice we used do not allow us to discriminate occupancy of wildtype HTT (wtHTT) vs. mutant HTT (mHTT). Nonetheless, we reason that the WT-specific, Q111-specific, and Shared categories enable us to functionally discriminate between HTT-chromatin interactions lost and gained in *Htt*$^{Q111/+}$ mice, and we used these genotype bins in subsequent analyses.

Genotype-specific interactions of HTT with repressed and active chromatin domains

To explore a role for HTT in gene regulation, we compared the locations of HTT genomic occupancy to known genomic features using the ChipEnrich Bioconductor package (Huber et al., 2015; Yu et al., 2015) and

the ”known genes” track of mm9. First, we tested the hypothesis that HTT occupies regions proximal to transcription start sites (TSSs), similar to a transcription factor. This had been suggested previously based on ChIP-qPCR (Benn et al., 2008) and by protein-protein interactions of HTT with several site-specific transcription factors in the nucleus (Steffan et al., 2000). However, we found that only 12% of highly reproducible HTT ChIP-seq peaks were located in TSS-proximal annotation categories (promoter, 5’UTR and first exon/intron; Fig. 2A). In contrast, ChIP-seq of RNA polymerase II (*Polr2a*) generated in parallel from the same samples revealed genomic occupancy predominantly in genic regions (Fig. 2A). Though uncommon, certain TSS-proximal HTT peaks appeared to be quite robust and co-localized with active promoters in the mouse brain. Examples include HTT peaks near TSSs of the amino acid transporters *Slc38a2*, *Slc6a9* and *Slc6a6* (Fig. S2A-C), as well as near the TSS of *Neat1,* a long noncoding RNA whose expression has been described to be increased in HD (Sunwoo et al., 2017), and whose silencing is protective against in HD mouse models (Fig. S2D; (Cheng et al., 2018). Genomic occupancy of HTT both in and outside of TSS-proximal peaks suggests that HTT could play multiple roles in the nucleus, but TSS-proximal actions like those of a classical transcription factor appear to be a relatively minor pattern.

The predominant localization of HTT in intergenic regions led us to test an alternative hypothesis that HTT interacts with chromatin remodeling factors in distal regulatory regions (Dietz et al., 2015; Seong et al., 2010). We examined co-localization of HTT with chromatin states and with specific histone modifications in the mouse forebrain, using publicly available ChromHMM models (Ernst and Kellis, 2012) and ChIP-seq datasets from ENCODE (Consortium and The ENCODE Project Consortium, 2012; Davis et al., 2018) and other sources. Since HTT is known to interact with the PRC2 chromatin remodeling complex (Seong et al., 2010)), we specifically hypothesized that HTT peaks would overlap regions of histone H3 lysine 27 trimethylation (H3K27me3), the chromatin mark written by PRC2. H3K27me3 is primarily associated with facultative heterochromatin, while “bivalent” regions marked by both H3K27me3 and by an active chromatin mark histone H3 lysine 4 trimethylation (H3K4me3) correspond to poised promoters and enhancers. As predicted, we found significant co-localization between HTT and H3K27me3. This result was initially obtained using H3K27me3 ChIP-seq data from the mouse forebrain generated by the ENCODE Consortium. In an independent dataset from striatal medium spiny neurons (Wiles and Selker, 2017); Table S4; Fig. 2B), we confirmed associations of HTT peaks both with H3K27me3 regions and with bivalent H3K27me3 / H3K4me3 regions. All of these associations appeared strongest for WT-specific and Shared HTT peaks ($q < 0.05$), but they also reached nominal levels of significance for Q111-specific HTT peaks. We also found nominally significant enrichments of WT-specific but not Shared or Q111-specific HTT peaks in facultative chromatin and bivalent TSS chromatin states from a 15-state ChromHMM chromatin segmentation model of the mouse forebrain produced by the ENCODE Consortium. These results suggest HTT genomic occupancy co-localizes with H3K27me3, especially in wildtype mice.

Expanding our analysis to additional chromatin states and chromatin modifications, we discovered strong, genotype-specific associations of HTT peaks with additional chromatin states and histone

modifications. WT-specific, Q111-specific, and Shared HTT peaksets were all strongly enriched in constitutive heterochromatin and with heterochromatin-associated histone H3 lysine 9 trimethylation, H3K9me3 (Fig. 2B, Table S4, all p-values < 1.0e-5; (ENCODE Project Consortium, 2012). For example, we observed tight co-localization of H3K9me3 and HTT, but not input control samples, near the gene *Sfi1* homolog, spindle assembly associated (yeast) (*Sfi1*; Fig. 1H).

In addition, we identified a genotype-specific association of Q111-specific peaks with active chromatin states and with associated histone modifications (Fig. 2B, Table S4). Specifically, using data from mouse forebrain generated by ENCODE, we found that Q111-specific peaks were significantly enriched ($q < 0.05$) in active TSSs, TSS-flanking regions, and enhancers, none of which were even nominally enriched at WT-specific or Shared peaks. Q111-specific peaks were also enriched at regions of H3K27 acetylation (H3K27ac) and H3K4 trimethylation (H3K4me3), both of which are associated with active promoters; in regions of H3K4 monomethylation (H3K4me1), which is associated with active enhancers; and in DNase I hypersensitive sites, which mark diverse open chromatin states. We replicated these findings using several additional H3K27ac and H3K4me3 ChIP-seq datasets from mouse striatum, consistently observing strong enrichments for Q111-specific HTT peaks, but not for WT-specific or Shared peaks. Overall, these analyses reveal that WT-specific and Shared HTT peaks are highly enriched in repressed chromatin regions, including constitutive heterochromatin, facultative heterochromatin, and poised promoters, whereas Q111-specific peaks are also uniquely enriched in active promoters and enhancers.

Histone Methylation and EZH2 Occupancy in *Htt*$^{Q111/+}$ mice

To directly compare HTT occupancy and chromatin states of interest, we generated ChIP-seq of H3K27me3 and H3K4me3 and of enhancer of zeste 2 (EZH2), the enzymatic component of the PRC2 complex (n = 3 / genotype). These experiments used striatal tissue from mice of the same age and genotype as the animals used for our HTT ChIP-seq experiments described above. After library construction, sequencing, input normalization and peak calling (Methods), we identified 17,894, 26,090, and 12,812 reproducible peaks for H3K4me3, H3K27me3, and EZH2, respectively.

Using these data, we first examined differential methylation / occupancy of each histone modification or protein in *Htt*$^{Q111/+}$ vs. *Htt*$^{+/+}$ samples. We identified 42 H3K27me3 differentially methylated regions (DMRs) at FDR < 0.1 (Table S6, Fig. 3A). At this statistical threshold, there were no DMRs for H3K4me3 or EZH2, suggesting that genotypic differences in these marks are more subtle or variable. Notably, 41 of 42 H3K27me3 DMRs (98%) had reduced levels of methylation in *Htt*$^{Q111/+}$ vs. *Htt*$^{+/+}$ samples ($\log_2(FC) < 0$; Fig. 3A, Table S6). Moreover, 1,926 of 2,018 H3K27me3 DMRs at a more lenient p-value < 0.05 (96%) had reduced methylation in *Htt*$^{Q111/+}$ samples. These results suggest that HD mutations cause substantial changes in H3K27 methylation in the 4-month-old *Htt*$^{Q111/+}$ striatum, including a previously undescribed reduction in H3K27me3 levels in many genomic regions.

Next, we attempted to replicate the enrichments of each histone modification or protein at genotype-specific HTT peaks. We confirmed that H3K27me3 peaks were specifically enriched at WT-specific (Fig. 3B, Table S5, logFC = 1.0, $p < 1e-5$), but not Q111-specific or Shared HTT peaks ($p > 0.05$). We also confirmed that H3K4me3 peaks were enriched specifically at Q111-specific HTT peaks (Fig. 3B, Table S5, H3K4me3: logFC = 1.4, $p < 1e-5$) and not at WT-specific or Shared HTT peaks ($p > 0.05$). These results further demonstrate the robustness of these genotype-specific associations of HTT peaks with repressed and active chromatin states. Interestingly, in contrast to H3K27me3, EZH2 peaks were enriched specifically at Q111-specific HTT peaks (Fig. 3B, Table S5, logFC = 1.6, $p < 1e-5$) and not at WT-specific or Shared HTT peaks ($p > 0.05$). This latter finding may indicate differences in the association of HTT with sites of active EZH2-containing PRC2 complexes vs. with stably methylated H3K27.

The global reduction of H3K27me3 in *Htt*$^{Q111/+}$ vs. *Htt*$^{+/+}$ striata suggested a possible partial change of PRC2 function. We studied the genes proximal to H3K27me3 DMRs (p-value < 0.05) to gain insight into their potential biological consequences. Functional annotation of H3K27me3 DMRs with GREAT (McLean et al., 2010) revealed that negative DMRs were enriched near genes that impinge on developmentally relevant biological processes (Fig. 3D, Table S7) including "anatomical structure regression" (GO:0060033; Bonferroni-corrected p-value = 1.5e-5) and "anatomical structure formation involved in morphogenesis" (GO:0048646; Bonferroni-corrected p-value = 5.3e-5). Negative H3K27me3 DMRs were also enriched near known PRC2 target genes, many of which are involved in cell fate determination (Table S6). Notable examples of developmentally important genes near negative H3K27me3 DMRs include the TFs *Mycn*, *Mycs*, *Sox11* and *Foxp2.* Reduced H3K27me3 levels in the vicinity of developmentally important genes may cause transcriptional derepression in the striata of young *Htt*$^{Q111/+}$ mice.

The results above indicate genotype-specific associations of HTT occupancy with H3K27me3, as well as genotype-specific changes in H3K27me3. Integrating these results, we hypothesized that genotype-specific changes in HTT occupancy and in H3K27me3 levels may colocalize in the genome. Indeed, WT-specific HTT peaks were enriched in DMRs with decreased H3K27me3 in *Htt*$^{Q111/+}$ vs. wildtype mice (Fig. 4E; $\log_2$(FC)= 1.7, p = 1.0e-5). The converse enrichment was also significant: Q111-specific HTT peaks were enriched in the rare DMRs with increased H3K27me3 in *Htt*$^{Q111/+}$ mice (Fig. 4E; $\log_2$(FC)= 3.3, p = 3.4e-2). Both results suggest that genotype-specific Huntingtin occupancy within a region predicts increased H3K27me3 levels in the same region.

Genotype-specific HTT occupancy predicts effects of HD mutations on histone modifications and gene expression

The genotype-specific association of HTT with active and repressed gene regulatory chromatin states raised the possibility that HTT may directly contribute to HD-related changes in gene expression. We mapped

potential HTT "target" genes whose TSSs were located within +/- 20 kb of an HTT ChIP peak. Assigning regulatory elements to their target genes is inevitably inexact, but previous work has shown that summing the regulatory elements within 20 kb of a TSS optimizes sensitivity and specificity for detecting gene regulatory interactions (Plaisier et al., 2016). This analysis revealed 3,120 HTT target genes, including 2,203 genes, 471 genes, and 709 genes near WT-specific, Shared, and Q111-specific HTT peaks, respectively (some genes overlap between categories; Fig. 4A). We then studied the enrichment of these HTT target genes in published lists of differentially expressed genes (DEGs) in the striatum of *Htt*$^{Q111/+}$ mice and in related knock-in mouse models from an HD allelic series (Langfelder et al., 2016). Q111-specific HTT peaks were enriched in the regions +/- 20 kb from the TSSs of genes down-regulated in HD knock-in mice (Fig. 4A; Table S4; $\log_2$(FC) = 1.21, p-value = 0.0004) and depleted near up-regulated genes (Fig. 4A; Table S4; $\log_2$(FC) = -1.53, p-value = 0.03). No robust enrichments between peaks in the other genotype bins and HD-associated DEGs were observed.

Next, we broadened this investigation to a collection of 2,194 manually curated HD-relevant transcriptional signatures in the Huntington's Disease Molecular Signatures Database (HDSigDB; https://hdsigdb.hdinhd.org/). We found significant overlap (q-value < 0.05) between 154, 283 and 166 HDSigDB gene sets and the WT-, Q111-specific and shared peak bins, respectively (Table S8), with many terms showing genotype-specific enrichments for HTT peaks (Fig. 4C). For Q111-specific peaks, most of the top HDSigDB gene sets were lists of genes down-regulated in HD and HD mouse models, replicating and extending the findings above. For instance, we found strong enrichment of Q111-specific peaks near genes of the "M2" co-expression module (Langfelder et al., 2016); Fig. 4C; $\log_2$(FC) = 1.3, p < 1e-5), the transcriptional module most tightly linked to CAG size in HD knock-in mice, which includes many genes expressed specifically in striatal medium spiny neurons. Potential HTT target genes in the M2 module include *Slc6a6*, which has TSS-proximal HTT peaks that are primarily in the Q111-specific peakset (Fig. S2B). For WT-specific peaks, the most robust HDSigDB enrichments included genes proximal to H3K27me3-rich regions in MSNs of adult mice (Fig. 4C; Log_2(FC)=0.8, p < 1e-5), as well as a DNA repair pathway, "Nucleotide Excision Repair Step 3: DNA Damage Verification and Incision" (Fig. 4C; Log_2(FC)=3.3, p = 4e-4). Notably, many of these DNA repair and H3K27me3-enriched genes near WT-specific peaks are up-regulated in HD knock-in mice. These results suggest that in the striatum, genes with large numbers of proximal Q111-specific peaks tend to be striatal neuronal identity genes, whose expression is downregulated during aging in HD knockin mice. On the other hand, genes with wildtype-specific peaks include striatal genes bearing H3K27me3 marks and DNA repair genes, whose expression is increased during aging in HD. In both cases, HTT occupancy is associated with decreased expression of nearby genes.

We hypothesized that the negative correlation between HTT occupancy and HD-related gene expression may be mediated by PRC2 and histone modifications. To investigate this, we integrated our data on HTT occupancy, histone modifications, and transcription, focusing on the genomic regions proximal to DEGs in 6-month-old *Htt*$^{Q111/+}$ versus *Htt*$^{Q20/+}$ mice (Fig. 5A-C, Table S9; (Langfelder et al., 2016). We defined

intervals of interest +/- 20 kb of the TSS of each HD DEG, and calculated the $\log_2$(FC) in *Htt*$^{Q111/+}$ vs. *Htt*$^{+/+}$ mice for HTT, H3K27me3, H3K4me3, and EZH2, all in that same interval. Consistent with our hypothesis, the fold changes in HTT occupancy in these regions were positively correlated with the fold changes in H3K27me3 levels (Fig. 5A, Table S9; Spearman's rho = 0.42, p = 7.0e-6), while the fold changes in EZH2 occupancy showed a trend in the same direction (Table S9; Fig. 5B; Spearman's rho = 0.12, p = 0.10). By contrast, the fold changes in HTT occupancy were negatively correlated with the fold changes in H3K4me3 levels in these same intervals (Fig. 5C, Table S9; rho = -0.35, p = 4.8e-3). Importantly, these relationships appeared to hold true both for up- and down-regulated genes in *Htt*$^{Q111/+}$ mice. Thus, concordant changes in PRC2 localization and histone methylation may mediate direct repression of HD-related genes by HTT in both *Htt*$^{Q111/+}$ and *Htt*$^{+/+}$ mice

Discussion

This study was motivated by the question of whether transcriptional dysregulation in Huntington's disease could be occurring due to direct interactions between HTT and chromatin. ChIP-seq of the HTT protein revealed thousands of robust and reproducible sites of HTT genomic occupancy in the mouse striatum, the brain region that is most vulnerable to HD pathology and in which the most pronounced transcriptional dysregulation occurs (Ament et al., 2017; Langfelder et al., 2016). We find that HTT peaks preferentially observed in *Htt*$^{Q111/+}$ mice are enriched near down-regulated genes in HD, and depleted near up-regulated genes, suggesting a link between HTT-chromatin interactions and transcriptional dysregulation in HD. We complemented these findings with ChIP-seq of histone-modifications, which revealed previously undescribed changes in histone methylation in the striatum of young *Htt*$^{Q111/+}$ mice. Integrating these datasets revealed a striking positive correlation between HTT occupancy and local levels of H3K27me3 and EZH2, and negative correlations with H3K4me3 levels. We believe these data support a mixed gain- and loss-of-function model for HTT in transcriptional dysregulation, which includes derepression of stress pathways, including DNA damage genes, accompanied by aberrant repression of striatal identity genes.

Most HTT peaks were intergenic, enriched at locations of both facultative and constitutive heterochromatin regions. Combined with prior evidence from protein-protein interactions, these data suggest that HTT interacts with chromatin modifying complexes that mediate the formation of heterochromatin and potentially plays a direct role in gene repression. An interaction of HTT with the PRC2 complex and H3K27me3 is supported by multiple lines of evidence and is discussed below. In addition, we found a robust enrichment of HTT peaks in H3K9me3-positive, constitutive, heterochromatin (Becker et al., 2016). This interaction is also supported by prior evidence. Wildtype HTT has been shown to suppress H3K9me3 formation in human embryonic stem cells (hESCs) via stabilization of an ATF7IP-SETDB1 complex, a role that is perturbed by polyglutamine expansion (Irmak et al., 2018). Consistent with HTT playing a polyQ-sensitive role in establishing constitutive heterochromatin, the brains of HD patients have increased H3K9me3 levels compared

to controls (Gardian et al., 2005; Lee et al., 2013; Ryu et al., 2006). Our data do not support a differential interaction between constitutive heterochromatin and wildtype versus mHTT, but are limited by being collected at a single – very early – time point. Interestingly, in *Drosophila*, wild-type Huntingtin loss modifies position-effect variegation phenotypes, caused by alterations in heterochromatin spread (Dietz et al., 2015) . The proposed mechanism for this is effect on variegation is modulation of the activity of the lysine-specific demethylase 1 (dLsd1) which demethylates H3K4, as a obligate preparatory step enabling trimethylation of H3K9 by SU(VAR)3-9 (Rudolph et al., 2007). These published studies suggest HTT plays a role at setting boundaries of constitutive heterochromatin via modulation of both H3K4me3 and H3K9me3 levels. Our results demonstrate that HTT occupancy is positively correlated with H3K27me3 and negatively correlated with H3K4me3, supporting the importance of HTT activating repressed genes, and suggest that future work focused on understanding the specific mechanisms by which HTT influences the balance between facultative and constitutive heterochromatin are of great interest.

Amongst transcriptional changes in the striatum of HD patients and animal models, a consistent feature is the down-regulation of striatal neuronal identity genes (Ament et al., 2017; Hodges et al., 2006; Langfelder et al., 2016). Several mechanisms have been proposed to explain these changes, including repression of striatal super-enhancers via reduced expression of enhancer RNAs (eRNA; (Le Gras et al., 2017), as well as de-repression of genes responsible for alternative cell fates via dysfunction of PRC2 (von Schimmelmann et al., 2016). Our results support both hypotheses. Support for the former mechanism is derived from the enrichment of Q111-specific peaks in active, open chromatin regions, accompanied by down-regulation of nearby genes. Support for the latter hypothesis is derived from the enrichment of HTT peaks, particularly wildtype-specific peaks, near genes marked with H3K27me3 (Fig. 3). These data suggest that HTT's function, and mHTT's dysfunction, may contribute to chromatin remodeling associated with aberrant expression of PRC2 target genes. This proposed role for HTT in activation of PRC2 target genes is bolstered by our histone modification and EZH2 occupancy data, which reveal reduced H3K27me3 signal in young *Htt*$^{Q111/+}$ mice (Fig. 3A), that parallel reduced HTT occupancy (Fig. 1C-E). In vivo support for the importance of HTT/PRC2 interactions comes from recent reports, which describe *increased* PRC2 binding to chromatin in mice overexpressing HTT (Bardile et al., 2019) and that silencing of H3K27me regulators, including *Setdb1*, exacerbates toxicity in multiple animal models of HD (Lee et al., 2013, 2017). Emerging data also support a key role for DNA damage and repair in the pathogenesis of HD – as variations in DNA mismatch repair genes are associated with both increases and decreases in average age of motor onset of HD (Genetic Modifiers of Huntington's Disease (GeM-HD) Consortium, 2015; Genetic Modifiers of Huntington's Disease (GeM-HD) Consortium., 2019). Here, we observe Wildtype-specific HTT peaks are enriched near nucleotide excision repair genes, suggesting reduced HTT occupancy at these loci when mHTT is present. These genes are upregulated in HD mouse model striata in a CAG dependent manner, suggesting aberrant up-regulation and/or derepression of these genes in cells expressing mHTT.

This study has a number of important limitations. As the first genome-wide map of HTT-chromatin interactions, it is possible - in fact, probable - that it contains both true interactions and false positives derived from background noise, antibody cross-reactivity and other sources of bias. We have tried to control for this by using a relatively large number of technical and biological replicates, however it seems likely that with increasing sensitivity and more replications we will find that only some of these peaks reflect true HTT-chromatin interactions. Another consideration is the reliance on specific antibodies, which limits us to establishing chromatin regions associated with specific epitopes of HTT. Future work using phospho-specific antibodies, and other dynamic epitopes are likely to nominate a different set of HTT-chromatin interactions, which are of great interest. Finally, our ChIP-seq experiments relied on bulk striatal tissue. It is likely that these changes have different magnitude and direction in different cell types, so emerging techniques enabling ChIP-seq of single cells and sorted cell populations (Rotem et al., 2015) should enable additional refinements of the findings presented here.

This work provides the first genome-wide map of HTT-chromatin interactions and identified key changes in these interactions due to HD mutations. It suggests that aberrant derepression of CAG-sensitive genes in HD samples - including cell identity and DNA repair genes - may be due to the direct molecular interactions of HTT and chromatin. We find that altered HTT-chromatin occupancy is accompanied by novel histone modification changes – notably, reductions in H3K27me3 – in the *Htt*$^{Q111/+}$ striata, which are associated with genotype-selective HTT occupancy in the same regions. In fact, the strength of HTT occupancy predicts increased H3K27me3 and EZH2 occupancy, and reductions in H3K4me3, consistent with a model in which HTT plays a functional role in regulating PRC2 activity, perhaps by helping recruit PRC2 to particular genomic loci. Collectively, our data support a model of pathogenesis in which perturbation of HTT's normal chromatin regulatory functions drives transcriptional dysregulation in HD leading to both up- and down-regulation of distinct classes of genes.

Acknowledgements

We thank Steven Henikoff, Peter Skene and Christine Codomo for library preparation of X-ChIP-seq samples and the Fred Hutchinson Cancer Research Center Genomics Shared Resource for sequencing. This work was supported by the CHDI Foundation (J.B.C., S.A.A.), a Huntington Society of Canada New Pathways grant (J.B.C.), and a National Science Foundation Graduate Research Fellowship to JRP.

Author Contributions

Conceptualization: JRP, LEH, NDP, SAA and JBC. Supervision: LEH, NDP, SAA and JBC. Investigation: DEB, HRP, JPC, RMB, SRC. Data Curation, Formal Analysis, and Visualization: ACS, JRP, DEB, SAA, JBC. Funding Acquisition: JBC, SAA. Writing – Original Draft: JBC, SAA. All authors reviewed and approved the final manuscript.

Declaration of Interests

JBC has received research support from Ionis Pharmaceuticals, Wave Life Sciences, Triplet Therapeutics and consulting fees from Skyhawk Therapeutics and Guidepoint. JBC is a member of the scientific advisory board of Triplet Therapeutics. None of these companies had any role in the design or interpretations of these experiments. Other authors report no conflicts.

Figure titles and Legends

Figure 1: Reproducible, genotype-specific, Huntingtin ChIPSeq peaks from 4-month-old *Htt*$^{+/+}$ and *Htt*$^{Q111/+}$ mice. A: Schematic of experimental design. B: Venn diagram depicting the number WT-specific, Q111-specific, and Shared HTT peaks reproducible at FDR < 0.01 in at least 3 biological replicates from each genotype. C-E. Volcano plots depicting the fold changes and p-values for differential occupancy of HTT in *Htt*$^{Q111/+}$ vs. *Htt*$^{+/+}$ striatum in each peak set. Peaks with negative fold-change values have greater occupancy in *Htt*$^{+/+}$ samples, and those with positive fold-change are greater in *Htt*$^{Q111/+}$ *samples.* F-G: Normalized genomic coverage at representative WT-specific (F), Q111-specific (G), and Shared (H) HTT peaks in *Htt*$^{+/+}$ mice (top 3 panels in orange), *Htt*$^{Q111/+}$ mice (middle 4 panels in blue), and merged input control samples (bottom 2 panels in purple). Signal tracks from ChIP-seq of H3K9me3, H3K27me3, H3K27ac, H3K4me3 in mouse forebrain at postnatal day 0 generated by the ENCODE Consortium are shown for comparison. At bottom, positions of RefSeq genes are indicated.

Figure 2: Huntingtin peaks occupy specific chromatin states. A: Summary of genomic regions occupied by HTT and RNAPolII peaks generated in the current study. HTT peaks, regardless of genotype of origin (bottom 3 rows), are less associated with genic annotation categories than RNAPolII peaks (top two rows). B: Enrichments of WT-specific, Shared, and Q111-specific HTT ChIP-seq peaks in chromatin states. Y-axis represents the z-score for enrichment or depletion in each chromatin state based on 100,000 permutations of genomic coordinates. Dotted line / gray bars = nominal significance ($p < 0.05$); Dashed line / red bars = Bonferroni adjusted significance ($p < 0.001$). At left, ChromHMM 15-state chromatin state model in postnatal C57BL/6 mouse forebrain, postnatal week (PW) 0. At right, individual chromatin marks from the following conditions: 1. forebrain, PW 0, C57BL/6 (ENCODE Project Consortium, 2012); 2. Striatal MSNs, PW8, C57BL/6. 3. Striatal MSNs, PRC2 knockout (von Schimmelmann et al., 2016); 4. Cortex, PW8, R6/2 mHTT transgenic (Vashishtha et al., 2013); 5. Cortex, PW8, C57BL/6 / CBA; 6. Cortex, PW12, R6/2 (transgenic mouse model of mHTT); 7. Cortex, PW12, C57BL/6 / CBA; 8. Striatum, PW8, R6/2 (transgenic mouse model of mHTT); 9. Striatum, PW8, C57BL/6 / CBA; 10. Striatum, PW12, R6/2 (transgenic mouse model of mHTT); 11. Striatum, PW12, C57BL/6 / CBA; 12. Striatum, PW30, R6/1 (Achour et al., 2015; Le Gras et al., 2017). Chromatin state abbreviations: Tx1, Tx2, transcribed regions; TssA, active transcription start sites (TSS);

TssAFlnk1, TssAFlnk2, TSS-flanking regions; TssBiv, bivalent TSS; Enh, enhancers; EnhLo1, EnhLo2, lower-activity enhancers;, EnhPois1, EnhPois2, poised enhancers; HetFac, facultative heterochromatin; HetCons, constitutive heterochromatin; Quies, QuiesG, quiescent.

Figure 3. Histone methylation analysis reveals early changes in H3K27me3 near developmentally important genes in *Htt*$^{Q111/+}$ mice. A: Volcano plots summarizing differentially histone modifications for H3K27me3 and H3K4me3 and differential occupancy for EZH2 in striatal tissue from four-month-old in *Htt*$^{Q111/+}$ vs. *Htt*$^{+/+}$ mice. The x-axis indicates the $\log_2$FC and the y-axis indicates the -$\log_{10}$(p-value). Regions with greater levels or occupancy in the *Htt*$^{+/+}$ mice are shown in orange, regions with lower levels/occupancy are indicated in blue. The dashed horizontal line indicates an FDR of 0.05, and the solid line represents a nominal p-value of 0.05. B: Enrichment of EZH2, H3K27me3 and H3K4me3 ChIP-seq peaks (MACS FDR < 0.05) at WT-specific, Q111-specific, and Shared HTT ChIP-seq peaks. Y-axis indicates the log-transformed fold change (enrichment or depletion) in the number of overlapping base pairs compared to the average from 100,000 re-sampling permutations of genomic coordinates. Plotting color indicates the p-value, derived from these same permutations. C: Gene Ontology Biological Processes enriched near differentially methylated regions with reduced H3K27me3 in *Htt*$^{Q111/+}$ mice (GREAT (McLean et al., 2010)). X-axis, p-value from binomial test over genomic regions; plot color, p-value from the hypergeometric test over genes results; plot size, hypergeometric test fold-enrichment.

Figure 4. Genotype-specific HTT occupancy in genomic regions surrounding HD DEGs and other CAG-sensitive gene sets of interest. A: Venn diagram showing counts of genes with a transcription start site +/- 20 kb from WT-specific, Q111-specific, and Shared HTT ChIP-seq peaks. B: Enrichment or depletion of Q111-specific, WT-specific, and Shared HTT ChIP-seq peaks in the regions +/- 20 kb from the transcription start sites of up- and down-regulated differentially expressed genes (DEGs) in the striatum of knock-in mouse models of HD mutations, based on RNA-seq from (Langfelder et al., 2016; Rotem et al., 2015). Y-axis indicates fold enrichment of base pair overlap compared to the average from 100,000 re-sampling permutations; * indicates enrichment p-value < 0.05. C: Heatmap showing HDSigDB gene sets enriched in the regions +/- 20 kb of WT-specific, Q111-specific, and Shared HTT ChIP-seq peaks. The plotting color indicates the -log10(p-value) for the strength of the enrichment, based on 100,000 re-sampling permutations. Rows are ordered by hierarchical clustering, based on p-values.

Figure 5. HTT occupancy is positively associated with H3K27me3 and EZH2, and negatively associated with H3K4me3, near genes that are dysregulated in HD. Each plot indicates the fold change of HTT occupancy in *Htt*$^{Q111/+}$ / *Htt*$^{+/+}$ mice (x-axis) compared to the fold change in the same regions for H3K27me3 (A), EZH2 (B), and H3K4me3 (C) (y-axis). Analysis is restricted to 263 HTT peaks located +/- 20 kb from the TSSs of genes that are significantly up- or down-regulated in the striatum of six-month-old knock-in mouse models of

HD mutations. Each point represents a single HTT ChIP-seq peak and is labeled with the name of the adjacent differentially expressed gene. Point color indicates the fold change in gene expression in the striatum of HD knock-in mice (up = yellow; down = purple), and point size corresponds to the p-value for differential expression.

Supplementary Information Titles and Legends

Supplementary figure 1: Treatment with a HTT-lowering ASO reduces HTT ChIPSeq peaks. S1A. Mice underwent unilateral intracerebroventricular injection with HTT-targeted ASO. Cortex ipsi- and contralateral to the injection were collected at four weeks post-injection. HTT lowering was assessed in contralateral cortex, while ChIP was performed on the ipsilateral cortex. S1B. Quantification of western blots probed with anti-HTT EPR5526 show HTT lowering of 53% in the contralateral cortex at four weeks post-ASO injection (ANOVA, Treatment effect p = 4.11x10^-9). Total number of reproducible peaks: 13,820 S1C. Volcano plot demonstrating 13,820 reproducible HTT-associated peaks in the cortex, 8,308 (60%) showing Log2(fold change) < 0 with ASO treatment. Likelihood that more than 50% had negative fold changes, p = 4.2x10^-126 (binomial test). Of differentially occupied peaks ($p < 0.05$): 502 out of 622 had negative fold changes (80%) with ASO treatment.

Supplemental Figure 2: High-confidence peaks near transcriptional start sites. S2A: IGV Screenshots showing HTT Peaks proximal to the TSSs of Slc38a2, Sodium-Coupled Neutral Amino Acid Transporter 2. S2B: HTT Peaks proximal to TSS in Slc6a6, Solute Carrier Family 6 (Neurotransmitter Transporter, Taurine), Member 6. S2C: HTT Peaks proximal to TSS in Slc6a9, Solute Carrier Family 6 (Neurotransmitter Transporter, Glycine), Member 9. S2C: HTT Peaks proximal to TSS in Neat1, Nuclear Paraspeckle Assembly Transcript 1. For each gene, the tracks in green indicate the HTT occupancy from $Htt^{+/+}$ mice, those in red from $Htt^{Q111/+}$ mice, and the purple tracks indicate input control (IC) binding. Below the HTT tracks is shown the ENCODE brain ChIPSeq signal tracks for H3K9me3 (blue), H3K27me3 (yellow), H3K4me3 and H3K4me1 (both green) and H3K27ac (red). Refseq gene annotations are shown below the ChIPSeq tracks, in blue.

Supplementary Table 1 – Peak calling results, including proximal gene names, for each sample. Each tab includes the MACS peak calling results - annotated with the most proximal gene and the distance to it - for a single sample. Sample names that include “PQ” arise from from $Htt^{Q111/+}$ mice, and those that include “WT" were generated from $Htt^{+/+}$ samples in parallel. The “EdgeR Results” tab includes assignment of peaks to peaksets (WT-specific, Q111-specific or Shared).

Supplementary Table 2 – HTT ChIPSeq antibody comparison results. Includes the GAT analysis and Jaccard statistics for the comparison of HTT ChIPSeq results generated with two antibodies (MAB2166 and EPR5526).

Supplementary Table 3 – ASO Treatment DiffBind Results. Contains the results of an analysis with DiffBind of the ASO-treated cohort of animals, including statistical analyses of genotypes and the effect of ASO treatment used to generate Fig. S1.

Supplementary Table 4 – GAT-derived Huntingtin peak set enrichments across other datasets. Includes enrichments for ENCODE-derived chromatin states and other genome-wide histone mark and gene expression datasets. These results were used to generate Fig. 2B.

Supplementary Table 5 – HTT Peaks in ActiveMotif Peaks. Includes a summary of the GAT results testing the enrichment of HTT ChIPSeq peaksets amongst H3K27me3, H3K4me3 and PRC peak regions. These results were used to generate Fig. 3B.

Supplementary Table 7 – GREAT Results for DiffBind nominated regions with differential ChIPSeq signal between *Htt*$^{+/+}$ and *Htt*$^{Q111/+}$ mice. Results of analyses carried out via GREAT investigating whether DiffBind nominated regions are enriched in specific gene ontology (GO) and other functional categories. Each tab includes data on a single mark, and a single log2FC sign (e.g. “H3K27me3_LFC_lt0” refers to regions with nominally decreased H3K27me3 in the *Htt*$^{Q111/+}$ samples). These results were used to generate Fig. 3C.

Supplementary Table 8 - HTT HDSigDB Overlap. Includes enrichments for HTT Peak sets and the genes included in each HDSigDB gene set. HDSigDB gene set meta information is included on the tab “HDSigDB.Genesets”. These results were used to generate Fig. 4C.

Supplementary Table 9 - HTT Peaks, ActiveMotif and RNASeq Integration. Includes integrated ChIPSeq and RNASeq data for all intervals containing robust HTT peaks. For each HTT peak (“PeakRegion.ID”), available changes in RNA expression of included genes (“Langfelder et. al. RNA-Seq”) and our other ChIPSeq data (“Re-analysis of ActiveMotif ChIP-Seq”) are shown. These results were used to generate Fig. 5A-C.

Methods

Mouse Breeding, Genotyping, and microdissection. The B6.*Htt*$^{Q111/+}$ mice (Strain 003456; JAX) used for the ChIP-seq study have a targeted mutation replacing mouse *Htt* exon 1 with the corresponding portion of human

HTT exon 1, including an expanded CAG tract. The targeted *Htt* allele was placed from the CD-1 background onto the C57BL/6J genetic background by selective backcrossing for more than 10 generations to the C57BL/6J strain at Jackson laboratories. Cohorts of heterozygote and wild-type littermate mice were generated by crossing B6.$Htt^{Q111/+}$ and B6.$Htt^{+/+}$ mice. Male mice were sacrificed at four months of age via a sodium phenobarbital based euthanasia solution (Fatal Plus, Henry Schein). Brain tissues were snap frozen in liquid nitrogen and stored in -80°C until ChIP was performed. Experiments were performed following NIH animal care guidelines and approved by Western Washington University's Institutional Animal Care and Use Committee under protocols 14-005 and 16-011.

Huntingtin knockdown in cortex. Four-month-old male mice underwent unilateral intracerebroventricular injection of 500ug pan-huntingtin antisense oligonucleotide (Ionis #444652) or received no treatment. Tissue was collected as above at four weeks post-injection; a time shown to have maximal HTT reduction in BACHD mice (Kordasiewicz et al., 2012). Cortical tissue contralateral to the injection was used to assess HTT knockdown by western blot (Coffey et al., 2017), and ipsilateral tissue was used for ChIP as performed below.

HTT ChIP-seq. We prepared replicate (n = 3-4 depending on genotype and antibody) ChIP samples using an anti-Huntingtin antibody from four-month-old $Htt^{Q111/+}$ and from age-matched $Htt^{+/+}$ mice. For each ChIP preparation, chromatin DNA was prepared using the combined striatal tissue from both hemispheres of three mice. Preliminary experiments suggested that this was the minimal amount of material required to provide enough material for multiple IPs. Striata were transferred to a glass dounce on ice and homogenized in cold PBS with protease inhibitors. High-resolution X-ChIP-seq was performed as described (Skene and Henikoff, 2015), with slight modifications. IPs were performed using Abcam Anti-huntingtin antibody EPR5526 (#ab109115). Sequencing libraries were prepared from the isolated ChIP DNA and from input DNA controls as previously described (Orsi et al., 2015). Libraries were sequenced on an Illumina HiSeq 2500 sequencer to a depth of ~17-25 million paired-end 25 bp reads per sample. Sequence reads have been deposited in gene expression omnibus, accession GSE102750. For ASO-treated cortices, ChIP-Seq library preparation and sequencing reactions were conducted at GENEWIZ, Inc. (South Plainfield, NJ, USA). Sequencing was performed on an Illumina HiSeq 4000 using 2x150 Paired End (PE) configuration. Sequencing reads were aligned to the mouse genome (mm9) using HISAT2. Peak-calling was then performed with MACS2.2, scaling to the size of the input control library. The final set of reproducible peaks was obtained using the dba() function in the DiffBind R package, retaining peaks that were reproducible at FDR < 0.01 in at least two samples and excluding artifactual blacklist regions from ENCODE. Sequence reads have been deposited in gene expression omnibus, accession GSE102750.

Histone mark and EZH2 ChIP-seq. Fresh frozen striatal tissue from five male four-month-old $Htt^{Q111/+}$ and age-matched $Htt^{+/+}$ mice were pooled per replicate for n = 3 samples. Further processing was performed at

Active Motif (Carlsbad, CA). Tissue was fixed in 1% formaldehyde, lysed, and disrupted with a Dounce homogenizer. DNA was sonicated to an average fragment length of 300-500bp, and 25ug chromatin plus 200ng *Drosophila* spike-in chromatin was incubated with antibody targeting EZH2, H3K27me3 or H3K4me3 (Active Motif catalog numbers 39901, 39155 and 399159, respectively). Antibody against H2Av was also present in the reaction to ensure efficient pull-down of the spike-in chromatin. Complexes were captured using protein A agarose beads (Invitrogen). Illumina sequencing libraries were prepared from ChIP and Input DNA by end-polishing, dA-addition, and adaptor ligation. Libraries were quantified and sequenced on Illumina's NextSeq 500 (75nt single end reads).

Analysis of striatal HTT ChIP-seq data. For the primary striatal HTT ChIP-seq dataset, sequencing reads were aligned to the mouse genome (mm9) using bowtie2 (Langmead and Salzberg, 2012). Peak-calling on each sample was performed with MACS v2.1 (Zhang et al., 2008)**,** scaling each library to the size of the input DNA sequence library to improve comparability between samples. We retained peak regions with a significant MACS p-value (FDR < 0.01). Aligned sequence reads were concatenated by genotype, using 3 $Htt^{+/+}$ samples and 4 $Htt^{Q111/+}$ samples to produce a combined sample file. Peak-calling was performed with model-based analysis of ChIPSeq data (MACS; (Zhang et al., 2008) on the combined files, as described above. We filtered for significant peaks (FDR < 0.01) and removed artifactual blacklisted regions of the genome (ENCODE Project Consortium, 2012).

Analysis of cortex HTT ChIP-seq data. Sequencing reads were aligned to the mouse genome (mm9) using HISAT2. Aligned reads from the four ChIP libraries were down-sampled to the size of the smallest sequencing library using samtools view -s. Aligned reads from the Input genomic DNA of all four samples were merged into a single control BAM file. Peak-calling was then performed with MACS2.2, scaling to the size of the input control library. The final set of reproducible peaks was obtained using the dba() function in the DiffBind R package, retaining peaks that were reproducible at FDR < 0.01 in at least two samples and excluding artifactual blacklist regions from ENCODE (ENCODE Project Consortium, 2012). We then used dba.count() to count the reads in each peak region from each ChIP sample and from the control sample. Next, a generalized linear model was fit, using the dba.analyze() DESeq2 wrapper, and we performed log-ratio tests to estimate effects of ASO treatment on HTT occupancy in each peak region. Genotype was treated as a blocking factor. Control read counts were subtracted for each site in each sample before fitting the model. This experiment was underpowered to detect statistically significant changes in occupancy at individual peak regions. Therefore, our primary test was for global depletion of HTT occupancy in ASO-treated mice across peak regions. For this purpose, we computed one-sided binomial tests with binom.test(), comparing the number of peaks with increased vs. decreased occupancy.

Analysis of histone mark and EZH2 ChIP-seq. Reads were aligned consecutively to the mouse (mm10) and *Drosophila* (dm3) genomes using the BWA algorithm (default settings). The number of mouse alignments used in the analysis was scaled to the number of *Drosophila* spike-in alignments (Egan et al., 2016). Peak-calling was performed with MACS v2.1. We selected peaks that were reproducibly identified in at least two samples of the same genotype. For analyses of differential occupancy, reads mapped to each peak region were normalized to total library size. Generalized linear models and log-ratio tests were fit with edgeR to identify differentially methylated regions.

Enrichment of peaks in genomic regions and gene sets. Over-representation of HTT peaks in chromatin states, genomic regions marked by histone modifications, and gene sets were calculated using the Genomic Association Tester (GAT; (Heger et al., 2013)). GAT calculates the number of base pairs overlapping between two genomic annotations and estimates its fold enrichment and significance based on re-sampling permutations within the mappable genome. Results described in this manuscript are based on 100,000 re-sampling permutations. Accession numbers for comparison datasets are shown in the Key Resources Table. For ChromHMM and ChIP-seq comparison datasets, we downloaded published tables of peak regions frpm the ENCODE portal or from the Gene Expression Omnibus. Similarly, for analyses of gene sets, we downloaded gene lists from HDSigDB (https://www.hdinhd.org/2018/05/22/hdsigdb/), and we defined the regions of interest as +/- 20 kb of the canonical TSSs of the genes in each set.

Code and Data Availability. Code used in the analysis of ChIPseq data is publicly available: https://github.com/seth-ament/ament-carroll-collab. ChIP-seq data have been deposited in the Gene Expression Omnibus (GSE150747, GSE102750 and GSE150748). Processed ChIP-seq data, including peak locations (BED files) and genomic coverage (bigWig files), have been deposited in the Neuroscience Multi-Omic Archive (NemO Archive), where we have created a TrackHub, suitable for viewing in the UCSC Genome Browser: http://data.nemoarchive.org/other/grant/sament/sament/htt-chipseq/.

References

Achour, M., Le Gras, S., Keime, C., Parmentier, F., Lejeune, F.-X., Boutillier, A.-L., Néri, C., Davidson, I., and Merienne, K. (2015). Neuronal identity genes regulated by super-enhancers are preferentially down-regulated in the striatum of Huntington's disease mice. Hum. Mol. Genet. *24*, 3481–3496.

Ament, S.A., Pearl, J.R., Grindeland, A., St Claire, J., Earls, J.C., Kovalenko, M., Gillis, T., Mysore, J., Gusella, J.F., Lee, J.-M., et al. (2017). High resolution time-course mapping of early transcriptomic, molecular and cellular phenotypes in Huntington's disease CAG knock-in mice across multiple genetic backgrounds. Hum. Mol. Genet. *26*, 913–922.

Ament, S.A., Pearl, J.R., Cantle, J.P., Bragg, R.M., Skene, P.J., Coffey, S.R., Bergey, D.E., Wheeler, V.C., MacDonald, M.E., Baliga, N.S., et al. (2018). Transcriptional regulatory networks underlying gene expression changes in Huntington's disease. Mol. Syst. Biol. *14*, e7435.

Bardile, C.F., Garcia-Miralles, M., Caron, N.S., Rayan, N.A., Langley, S.R., Harmston, N., Rondelli, A.M., Teo, R.T.Y., Waltl, S., Anderson, L.M., et al. (2019). Intrinsic mutant HTT-mediated defects in oligodendroglia cause myelination deficits and behavioral abnormalities in Huntington disease. Proc. Natl. Acad. Sci. U. S. A. 201818042.

Bassi, S., Tripathi, T., Monziani, A., Di Leva, F., and Biagioli, M. (2017). Epigenetics of Huntington's Disease. In Neuroepigenomics in Aging and Disease, (Springer), pp. 277–299.

Becker, J.S., Nicetto, D., and Zaret, K.S. (2016). H3K9me3-Dependent Heterochromatin: Barrier to Cell Fate Changes. Trends Genet. *32*, 29–41.

Benn, C.L., Sun, T., Sadri-Vakili, G., McFarland, K.N., DiRocco, D.P., Yohrling, G.J., Clark, T.W., Bouzou, B., and Cha, J.-H.J. (2008). Huntingtin Modulates Transcription, Occupies Gene Promoters In Vivo, and Binds Directly to DNA in a Polyglutamine-Dependent Manner. Journal of Neuroscience *28*, 10720–10733.

Bragg, R.M., Coffey, S.R., Weston, R.M., Ament, S.A., Cantle, J.P., Minnig, S., Funk, C.C., Shuttleworth, D.D., Woods, E.L., Sullivan, B.R., et al. (2017). Motivational, proteostatic and transcriptional deficits precede synapse loss, gliosis and neurodegeneration in the B6.Htt/+Q111/+ model of Huntington's disease. Sci. Rep. *7*, 41570.

Cha, J.-H.J. (2007). Transcriptional signatures in Huntington's disease. Prog. Neurobiol. *83*, 228–248.

Cheng, C., Spengler, R.M., Keiser, M.S., Monteys, A.M., Rieders, J.M., Ramachandran, S., and Davidson, B.L. (2018). The long non-coding RNA NEAT1 is elevated in polyglutamine repeat expansion diseases and protects from disease gene-dependent toxicities. Hum. Mol. Genet. *27*, 4303–4314.

Coffey, S.R., Bragg, R.M., Minnig, S., Ament, S.A., Cantle, J.P., Glickenhaus, A., Shelnut, D., Carrillo, J.M., Shuttleworth, D.D., Rodier, J.-A., et al. (2017). Peripheral huntingtin silencing does not ameliorate central signs of disease in the B6.HttQ111/ mouse model of Huntington's disease. PLOS ONE *12*, e0175968.

Consortium, T.E.P., and The ENCODE Project Consortium (2012). An integrated encyclopedia of DNA elements in the human genome. Nature *489*, 57–74.

Davis, C.A., Hitz, B.C., Sloan, C.A., Chan, E.T., Davidson, J.M., Gabdank, I., Hilton, J.A., Jain, K., Baymuradov, U.K., Narayanan, A.K., et al. (2018). The Encyclopedia of DNA elements (ENCODE): data portal update. Nucleic Acids Research *46*, D794–D801.

Dietz, K.N., Di Stefano, L., Maher, R.C., Zhu, H., Macdonald, M.E., Gusella, J.F., and Walker, J.A. (2015). The Drosophila Huntington's disease gene ortholog dhtt influences chromatin regulation during development. Hum.

Mol. Genet. *24*, 330–345.

Egan, B., Yuan, C.-C., Craske, M.L., Labhart, P., Guler, G.D., Arnott, D., Maile, T.M., Busby, J., Henry, C., Kelly, T.K., et al. (2016). An Alternative Approach to ChIP-Seq Normalization Enables Detection of Genome-Wide Changes in Histone H3 Lysine 27 Trimethylation upon EZH2 Inhibition. PLOS ONE *11*, e0166438.

ENCODE Project Consortium (2012). An integrated encyclopedia of DNA elements in the human genome. Nature *489*, 57–74.

Ernst, J., and Kellis, M. (2012). ChromHMM: automating chromatin-state discovery and characterization. Nature Methods *9*, 215–216.

Gardian, G., Browne, S.E., Choi, D.-K., Klivenyi, P., Gregorio, J., Kubilus, J.K., Ryu, H., Langley, B., Ratan, R.R., Ferrante, R.J., et al. (2005). Neuroprotective effects of phenylbutyrate in the N171-82Q transgenic mouse model of Huntington's disease. J. Biol. Chem. *280*, 556–563.

Genetic Modifiers of Huntington's Disease (GeM-HD) Consortium (2015). Identification of Genetic Factors that Modify Clinical Onset of Huntington's Disease. Cell *162*, 516–526.

Genetic Modifiers of Huntington's Disease (GeM-HD) Consortium. (2019). CAG Repeat Not Polyglutamine Length Determines Timing of Huntington's Disease Onset. Cell *178*, 887–900.e14.

Gu, X., Cantle, J.P., Greiner, E.R., Lee, C.Y.D., Barth, A.M., Gao, F., Park, C.S., Zhang, Z., Sandoval-Miller, S., Zhang, R.L., et al. (2015). N17 Modifies mutant Huntingtin nuclear pathogenesis and severity of disease in HD BAC transgenic mice. Neuron *85*, 726–741.

Heger, A., Webber, C., Goodson, M., Ponting, C.P., and Lunter, G. (2013). GAT: a simulation framework for testing the association of genomic intervals. Bioinformatics *29*, 2046–2048.

Hodges, A., Strand, A.D., Aragaki, A.K., Kuhn, A., Sengstag, T., Hughes, G., Elliston, L.A., Hartog, C., Goldstein, D.R., Thu, D., et al. (2006). Regional and cellular gene expression changes in human Huntington's disease brain. Human Molecular Genetics *15*, 965–977.

Huber, W., Carey, V.J., Gentleman, R., Anders, S., Carlson, M., Carvalho, B.S., Bravo, H.C., Davis, S., Gatto, L., Girke, T., et al. (2015). Orchestrating high-throughput genomic analysis with Bioconductor. Nat. Methods *12*, 115–121.

Irmak, D., Fatima, A., Gutiérrez-Garcia, R., Rinschen, M.M., Wagle, P., Altmüller, J., Arrigoni, L., Hummel, B., Klein, C., Frese, C.K., et al. (2018). Mechanism suppressing H3K9 trimethylation in pluripotent stem cells and its demise by polyQ-expanded huntingtin mutations. Hum. Mol. Genet. *27*, 4117–4134.

Kordasiewicz, H.B., Stanek, L.M., Wancewicz, E.V., Mazur, C., McAlonis, M.M., Pytel, K.A., Artates, J.W., Weiss, A., Cheng, S.H., Shihabuddin, L.S., et al. (2012). Sustained Therapeutic Reversal of Huntington's Disease by Transient Repression of Huntingtin Synthesis. Neuron *74*, 1031–1044.

Langfelder, P., Cantle, J.P., Chatzopoulou, D., Wang, N., Gao, F., Al-Ramahi, I., Lu, X.-H., Ramos, E.M., El-Zein, K., Zhao, Y., et al. (2016). Integrated genomics and proteomics define huntingtin CAG length-dependent networks in mice. Nat. Neurosci. *19*, 623–633.

Langmead, B., and Salzberg, S.L. (2012). Fast gapped-read alignment with Bowtie 2. Nat. Methods *9*, 357–359.

Lee, J., Hwang, Y.J., Shin, J.-Y., Lee, W.-C., Wie, J., Kim, K.Y., Lee, M.Y., Hwang, D., Ratan, R.R., Pae, A.N., et al. (2013). Epigenetic regulation of cholinergic receptor M1 (CHRM1) by histone H3K9me3 impairs Ca2

signaling in Huntington's disease. Acta Neuropathologica *125*, 727–739.

Lee, J., Hwang, Y.J., Kim, Y., Lee, M.Y., Hyeon, S.J., Lee, S., Kim, D.H., Jang, S.J., Im, H., Min, S.-J., et al. (2017). Remodeling of heterochromatin structure slows neuropathological progression and prolongs survival in an animal model of Huntington's disease. Acta Neuropathologica *134*, 729–748.

Le Gras, S., Keime, C., Anthony, A., Lotz, C., De Longprez, L., Brouillet, E., Cassel, J.-C., Boutillier, A.-L., and Merienne, K. (2017). Altered enhancer transcription underlies Huntington's disease striatal transcriptional signature. Sci. Rep. *7*, 42875.

MacDonald, M.E., Ambrose, C.M., Duyao, M.P., Myers, R.H., Lin, C., Srinidhi, L., Barnes, G., Taylor, S.A., James, M., Groot, N., et al. (1993). A novel gene containing a trinucleotide repeat that is expanded and unstable on Huntington's disease chromosomes. Cell *72*, 971–983.

McLean, C.Y., Bristor, D., Hiller, M., Clarke, S.L., Schaar, B.T., Lowe, C.B., Wenger, A.M., and Bejerano, G. (2010). GREAT improves functional interpretation of cis-regulatory regions. Nat. Biotechnol. *28*, 495–501.

Neuwald, A.F. (2000). HEAT Repeats Associated with Condensins, Cohesins, and Other Complexes Involved in Chromosome-Related Functions. Genome Res. *10*, 1445–1452.

Orsi, G.A., Kasinathan, S., Zentner, G.E., Henikoff, S., and Ahmad, K. (2015). Mapping regulatory factors by immunoprecipitation from native chromatin. Curr. Protoc. Mol. Biol. *110*, 21.31.1–25.

Plaisier, C.L., O'Brien, S., Bernard, B., Reynolds, S., Simon, Z., Toledo, C.M., Ding, Y., Reiss, D.J., Paddison, P.J., and Baliga, N.S. (2016). Causal Mechanistic Regulatory Network for Glioblastoma Deciphered Using Systems Genetics Network Analysis. Cell Systems *3*, 172–186.

Robinson, M.D., McCarthy, D.J., and Smyth, G.K. (2010). edgeR: a Bioconductor package for differential expression analysis of digital gene expression data. Bioinformatics *26*, 139–140.

Rotem, A., Ram, O., Shoresh, N., Sperling, R.A., Goren, A., Weitz, D.A., and Bernstein, B.E. (2015). Single-cell ChIP-seq reveals cell subpopulations defined by chromatin state. Nature Biotechnology *33*, 1165–1172.

Rudolph, T., Yonezawa, M., Lein, S., Heidrich, K., Kubicek, S., Schäfer, C., Phalke, S., Walther, M., Schmidt, A., Jenuwein, T., et al. (2007). Heterochromatin Formation in Drosophila Is Initiated through Active Removal of H3K4 Methylation by the LSD1 Homolog SU(VAR)3-3. Mol. Cell *26*, 103–115.

Ryu, H., Lee, J., Hagerty, S.W., Soh, B.Y., McAlpin, S.E., Cormier, K.A., Smith, K.M., and Ferrante, R.J. (2006). ESET/SETDB1 gene expression and histone H3 (K9) trimethylation in Huntington's disease. Proceedings of the National Academy of Sciences *103*, 19176–19181.

Saudou, F., and Humbert, S. (2016). The Biology of Huntingtin. Neuron *89*, 910–926.

Saudou, F., Finkbeiner, S., Devys, D., and Greenberg, M.E. (1998). Huntingtin acts in the nucleus to induce apoptosis but death does not correlate with the formation of intranuclear inclusions. Cell *95*, 55–66.

von Schimmelmann, M., Feinberg, P.A., Sullivan, J.M., Ku, S.M., Badimon, A., Duff, M.K., Wang, Z., Lachmann, A., Dewell, S., Ma'ayan, A., et al. (2016). Polycomb repressive complex 2 (PRC2) silences genes responsible for neurodegeneration. Nat. Neurosci. *19*, 1321–1330.

Schut, M.H., Pepers, B.A., Klooster, R., van der Maarel, S.M., El Khatabi, M., Verrips, T., den Dunnen, J.T., van Ommen, G.-J.B., and van Roon-Mom, W.M.C. (2015). Selection and characterization of llama single domain antibodies against N-terminal huntingtin. Neurol. Sci. *36*, 429–434.

Seong, I.S., Woda, J.M., Song, J.-J., Lloret, A., Abeyrathne, P.D., Woo, C.J., Gregory, G., Lee, J.-M., Wheeler, V.C., Walz, T., et al. (2010). Huntingtin facilitates polycomb repressive complex 2. Hum. Mol. Genet. *19*, 573–583.

Skene, P.J., and Henikoff, S. (2015). A simple method for generating high-resolution maps of genome-wide protein binding. Elife *4*, e09225.

Steffan, J.S., Kazantsev, A., Spasic-Boskovic, O., Greenwald, M., Zhu, Y.Z., Gohler, H., Wanker, E.E., Bates, G.P., Housman, D.E., and Thompson, L.M. (2000). The Huntington's disease protein interacts with p53 and CREB-binding protein and represses transcription. Proc. Natl. Acad. Sci. U. S. A. *97*, 6763–6768.

Sunwoo, J.-S., Lee, S.-T., Im, W., Lee, M., Byun, J.-I., Jung, K.-H., Park, K.-I., Jung, K.-Y., Lee, S.K., Chu, K., et al. (2017). Altered Expression of the Long Noncoding RNA NEAT1 in Huntington's Disease. Mol. Neurobiol. *54*, 1577–1586.

Trottier, Y., Devys, D., Imbert, G., Saudou, F., An, I., Lutz, Y., Weber, C., Agid, Y., Hirsch, E.C., and Mandel, J.L. (1995). Cellular localization of the Huntington's disease protein and discrimination of the normal and mutated form. Nat. Genet. *10*, 104–110.

Vashishtha, M., Ng, C.W., Yildirim, F., Gipson, T.A., Kratter, I.H., Bodai, L., Song, W., Lau, A., Labadorf, A., Vogel-Ciernia, A., et al. (2013). Targeting H3K4 trimethylation in Huntington disease. Proc. Natl. Acad. Sci. U. S. A. *110*, E3027–E3036.

Wiles, E.T., and Selker, E.U. (2017). H3K27 methylation: a promiscuous repressive chromatin mark. Curr. Opin. Genet. Dev. *43*, 31–37.

Yu, G., Wang, L.-G., and He, Q.-Y. (2015). ChIPseeker: an R/Bioconductor package for ChIP peak annotation, comparison and visualization. Bioinformatics *31*, 2382–2383.

Zhang, Y., Liu, T., Meyer, C.A., Eeckhoute, J., Johnson, D.S., Bernstein, B.E., Nusbaum, C., Myers, R.M., Brown, M., Li, W., et al. (2008). Model-based analysis of ChIP-Seq (MACS). Genome Biol. *9*, R137.

Manuscript

Click here to access/download;Figure;ChIPSeq - Figures.pdf

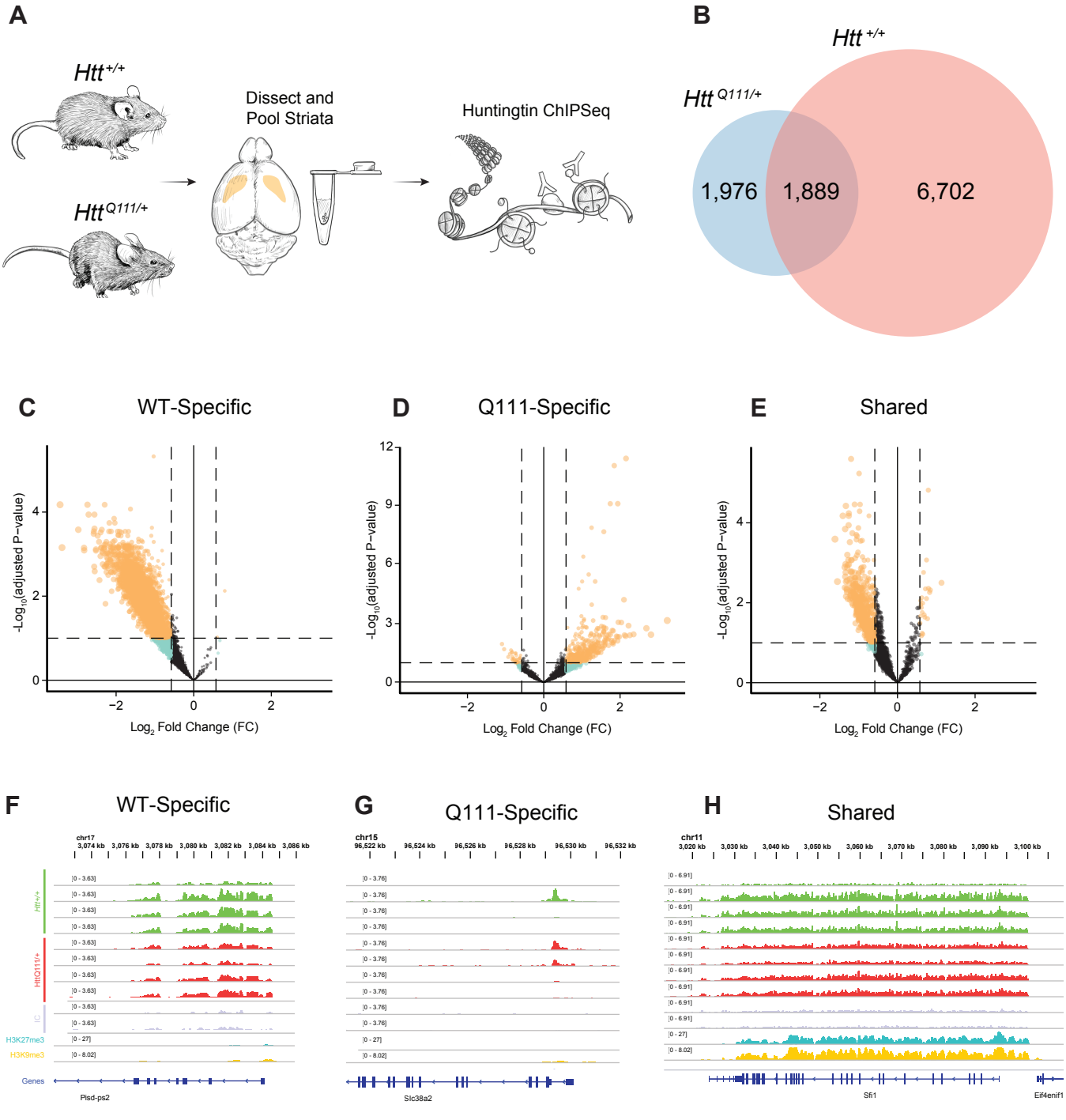

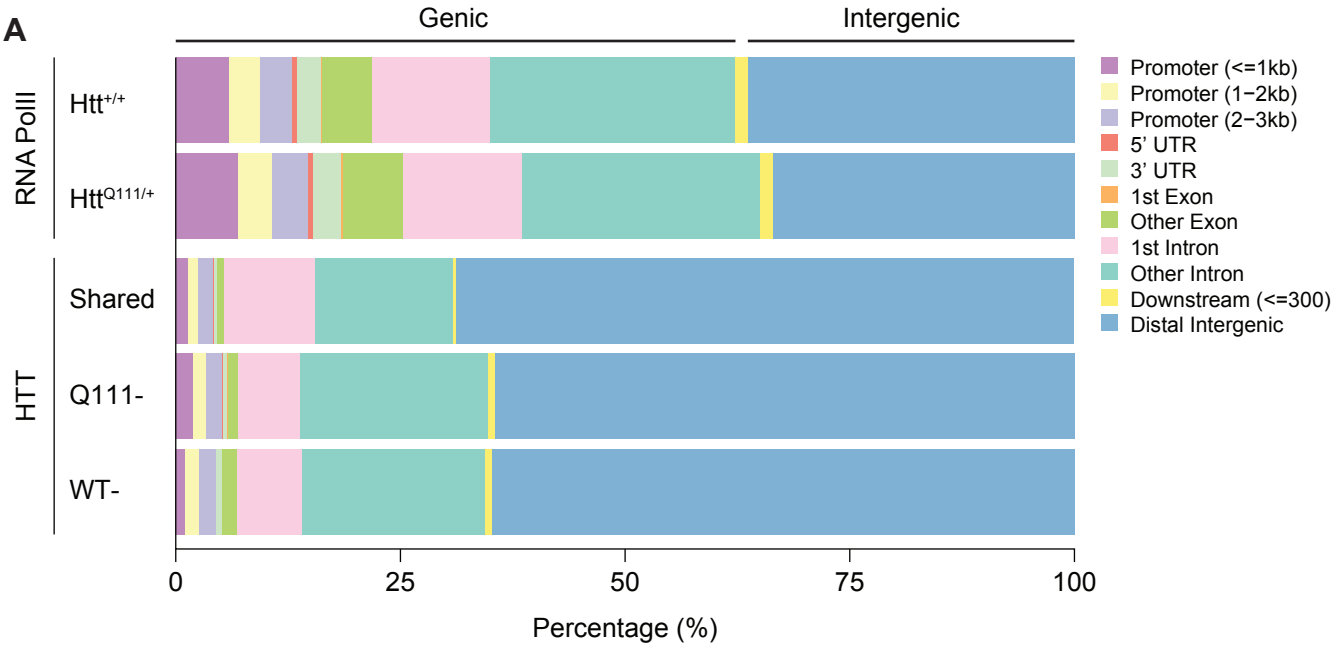
A
Genic
Intergenic
RNA PolII
Htt+/+
HttQ111/+
HTT
Shared
Q111-
WT-
0
25
50
75
100
Percentage (%)
Promoter (<=1kb)
Promoter (1−2kb)
Promoter (2−3kb)
5' UTR
3' UTR
1st Exon
Other Exon
1st Intron
Other Intron
Downstream (<=300)
Distal Intergenic

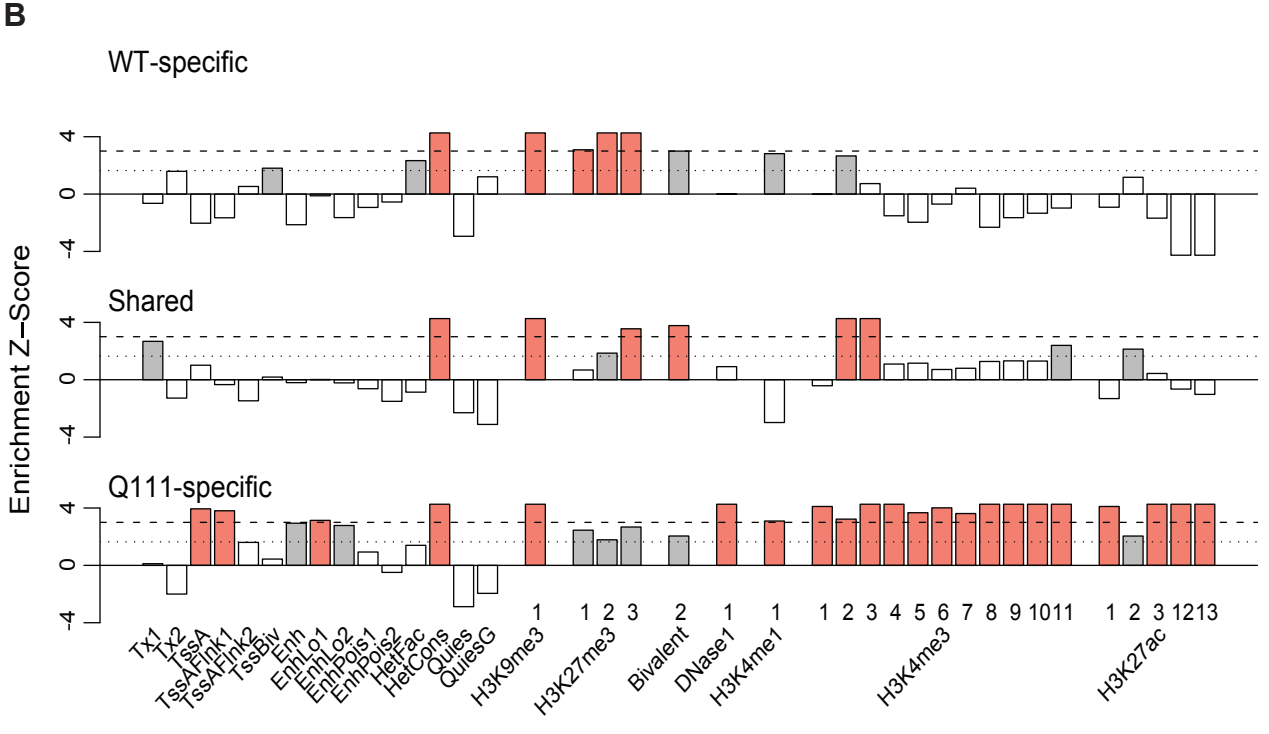
B
WT-specific
Shared
Q111-specific
Enrichment Z−Score
4
0
-4
Tx1
Tx2
TssA
TssAFlnk1
TssAFlnk2
TssBiv
Enh
EnhLo1
EnhLo2
EnhPois1
EnhPois2
HetFac
HetCons
QuiesG
H3K9me3
H3K27me3
Bivalent
DNase1
H3K4me1
H3K4me3
H3K27ac

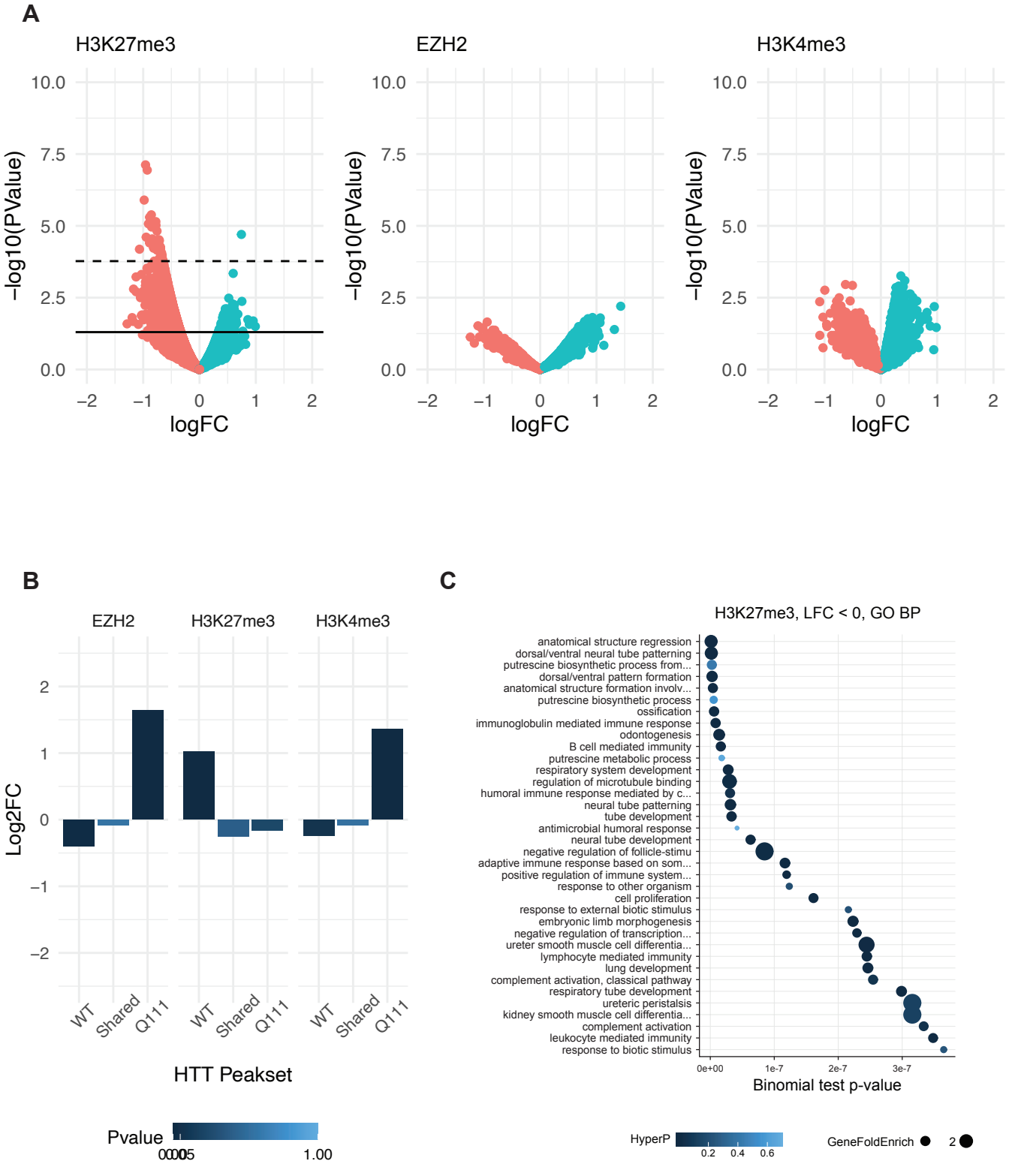
A
H3K27me3
EZH2
H3K4me3
−log10(PValue)
logFC
B
EZH2
H3K27me3
H3K4me3
Log2FC
WT
Shared
Q111
HTT Peakset
Pvalue
1.00
C
H3K27me3, LFC < 0, GO BP
anatomical structure regression
dorsal/ventral neural tube patterning
putrescine biosynthetic process from...
dorsal/ventral pattern formation
anatomical structure formation involv...
putrescine biosynthetic process
ossification
immunoglobulin mediated immune response
odontogenesis
B cell mediated immunity
putrescine metabolic process
respiratory system development
regulation of microtubule binding
humoral immune response mediated by c...
neural tube patterning
tube development
antimicrobial humoral response
neural tube development
negative regulation of follicle-stimu
adaptive immune response based on som...
positive regulation of immune system...
response to other organism
cell proliferation
response to external biotic stimulus
embryonic limb morphogenesis
negative regulation of transcription...
ureter smooth muscle cell differentia...
lymphocyte mediated immunity
lung development
complement activation, classical pathway
respiratory tube development
ureteric peristalsis
kidney smooth muscle cell differentia...
complement activation
leukocyte mediated immunity
response to biotic stimulus
0e+00
1e-7
2e-7
3e-7
Binomial test p-value
HyperP
0.2
0.4
0.6
GeneFoldEnrich
2

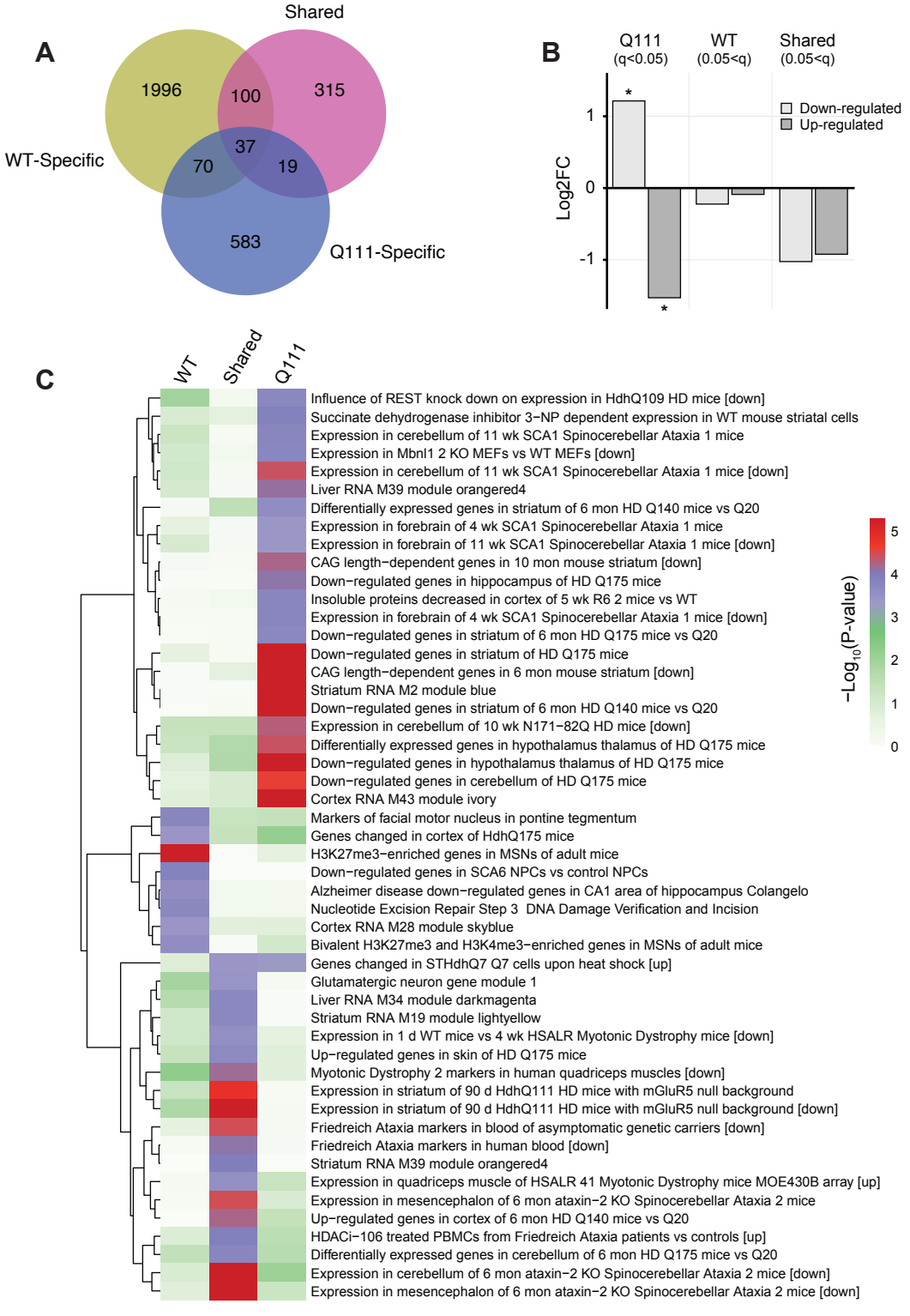
A
Shared
1996
100
315
WT-Specific
37
70
19
583
Q111-Specific
B
Q111
(q<0.05)
WT
(0.05<q)
Shared
(0.05<q)
Down-regulated
Up-regulated
Log2FC
1
0
-1
*
*
C
WT
Shared
Q111
Influence of REST knock down on expression in HdhQ109 HD mice [down]
Succinate dehydrogenase inhibitor 3−NP dependent expression in WT mouse striatal cells
Expression in cerebellum of 11 wk SCA1 Spinocerebellar Ataxia 1 mice
Expression in Mbnl1 2 KO MEFs vs WT MEFs [down]
Expression in cerebellum of 11 wk SCA1 Spinocerebellar Ataxia 1 mice [down]
Liver RNA M39 module orangered4
Differentially expressed genes in striatum of 6 mon HD Q140 mice vs Q20
Expression in forebrain of 4 wk SCA1 Spinocerebellar Ataxia 1 mice
Expression in forebrain of 11 wk SCA1 Spinocerebellar Ataxia 1 mice [down]
CAG length−dependent genes in 10 mon mouse striatum [down]
Down−regulated genes in hippocampus of HD Q175 mice
Insoluble proteins decreased in cortex of 5 wk R6 2 mice vs WT
Expression in forebrain of 4 wk SCA1 Spinocerebellar Ataxia 1 mice [down]
Down−regulated genes in striatum of 6 mon HD Q175 mice vs Q20
Down−regulated genes in striatum of HD Q175 mice
CAG length−dependent genes in 6 mon mouse striatum [down]
Striatum RNA M2 module blue
Down−regulated genes in striatum of 6 mon HD Q140 mice vs Q20
Expression in cerebellum of 10 wk N171−82Q HD mice [down]
Differentially expressed genes in hypothalamus thalamus of HD Q175 mice
Down−regulated genes in hypothalamus thalamus of HD Q175 mice
Down−regulated genes in cerebellum of HD Q175 mice
Cortex RNA M43 module ivory
Markers of facial motor nucleus in pontine tegmentum
Genes changed in cortex of HdhQ175 mice
H3K27me3−enriched genes in MSNs of adult mice
Down−regulated genes in SCA6 NPCs vs control NPCs
Alzheimer disease down−regulated genes in CA1 area of hippocampus Colangelo
Nucleotide Excision Repair Step 3 DNA Damage Verification and Incision
Cortex RNA M28 module skyblue
Bivalent H3K27me3 and H3K4me3−enriched genes in MSNs of adult mice
Genes changed in STHdhQ7 Q7 cells upon heat shock [up]
Glutamatergic neuron gene module 1
Liver RNA M34 module darkmagenta
Striatum RNA M19 module lightyellow
Expression in 1 d WT mice vs 4 wk HSALR Myotonic Dystrophy mice [down]
Up−regulated genes in skin of HD Q175 mice
Myotonic Dystrophy 2 markers in human quadriceps muscles [down]
Expression in striatum of 90 d HdhQ111 HD mice with mGluR5 null background
Expression in striatum of 90 d HdhQ111 HD mice with mGluR5 null background [down]
Friedreich Ataxia markers in blood of asymptomatic genetic carriers [down]
Friedreich Ataxia markers in human blood [down]
Striatum RNA M39 module orangered4
Expression in quadriceps muscle of HSALR 41 Myotonic Dystrophy mice MOE430B array [up]
Expression in mesencephalon of 6 mon ataxin−2 KO Spinocerebellar Ataxia 2 mice
Up−regulated genes in cortex of 6 mon HD Q140 mice vs Q20
HDACi−106 treated PBMCs from Friedreich Ataxia patients vs controls [up]
Differentially expressed genes in cerebellum of 6 mon HD Q175 mice vs Q20
Expression in cerebellum of 6 mon ataxin−2 KO Spinocerebellar Ataxia 2 mice [down]
Expression in mesencephalon of 6 mon ataxin−2 KO Spinocerebellar Ataxia 2 mice [down]
−Log10(P-value)
5
4
3
2
1
0

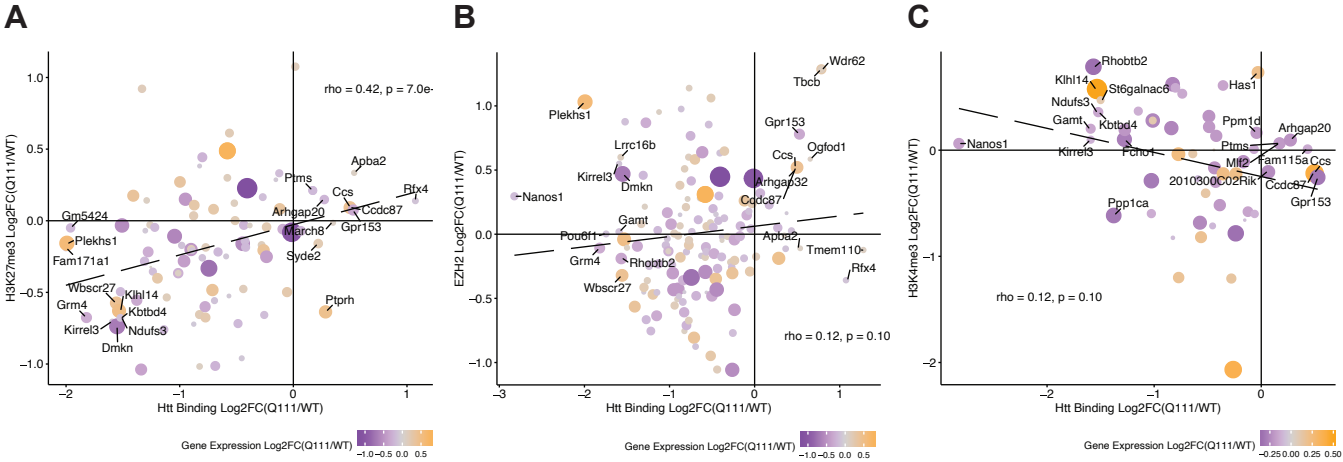
A
rho = 0.42, p = 7.0e-
H3K27me3 Log2FC(Q111/WT)
Htt Binding Log2FC(Q111/WT)
Apba2
Ptms
Ccs
Rfx4
Arhgap20
Ccdc87
Gpr153
March8
Syde2
Gm5424
Plekhs1
Fam171a1
Wbscr27
Klhl14
Grm4
Kbtbd4
Kirrel3
Ndufs3
Dmkn
Ptprh
Gene Expression Log2FC(Q111/WT)
B
Wdr62
Tbcb
Plekhs1
Gpr153
Lrrc16b
Ogfod1
Ccs
Kirrel3
Dmkn
Arhgap32
Nanos1
Ccdc87
Gamt
Pou6f1
Apba2
Tmem110
Grm4
Rhobtb2
Rfx4
Wbscr27
rho = 0.12, p = 0.10
EZH2 Log2FC(Q111/WT)
Htt Binding Log2FC(Q111/WT)
Gene Expression Log2FC(Q111/WT)
C
Rhobtb2
Klhl14
St6galnac6
Has1
Ndufs3
Gamt
Kbtbd4
Ppm1d
Arhgap20
Nanos1
Kirrel3
Fcho1
Ptms
Mlf2
Fam115a
Ccs
2010300C02Rik
Ccdc87
Gpr153
Ppp1ca
rho = 0.12, p = 0.10
H3K4me3 Log2FC(Q111/WT)
Htt Binding Log2FC(Q111/WT)
Gene Expression Log2FC(Q111/WT)

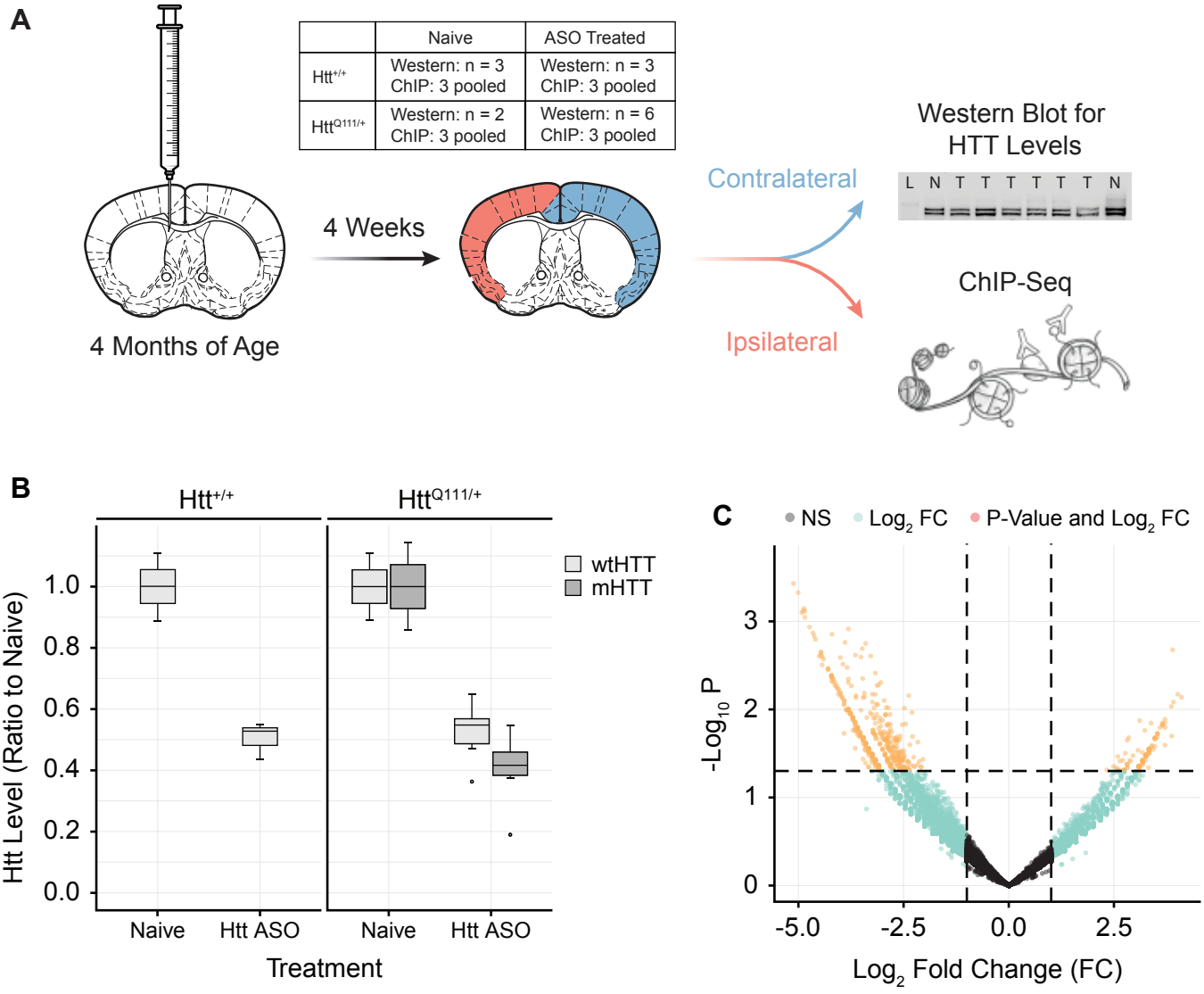
A
Naive
ASO Treated
Htt+/+
Western: n = 3
ChIP: 3 pooled
Western: n = 3
ChIP: 3 pooled
HttQ111/+
Western: n = 2
ChIP: 3 pooled
Western: n = 6
ChIP: 3 pooled
4 Months of Age
4 Weeks
Contralateral
Ipsilateral
Western Blot for HTT Levels
L N T T T T T T N
ChIP-Seq
B
Htt+/+
HttQ111/+
wtHTT
mHTT
Htt Level (Ratio to Naive)
1.0
0.8
0.6
0.4
0.2
0.0
Naive
Htt ASO
Naive
Htt ASO
Treatment
C
NS
Log2 FC
P-Value and Log2 FC
-Log10 P
3
2
1
0
-5.0
-2.5
0.0
2.5
Log2 Fold Change (FC)

A *Slc38a2*

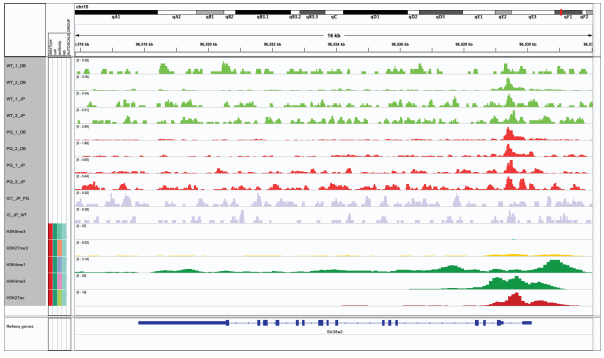

B *Slc6a6*

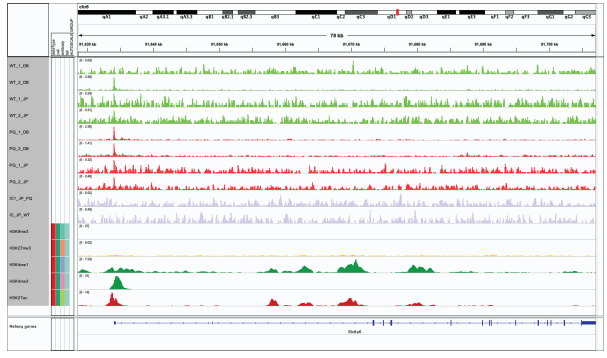

C *Slc6a9*

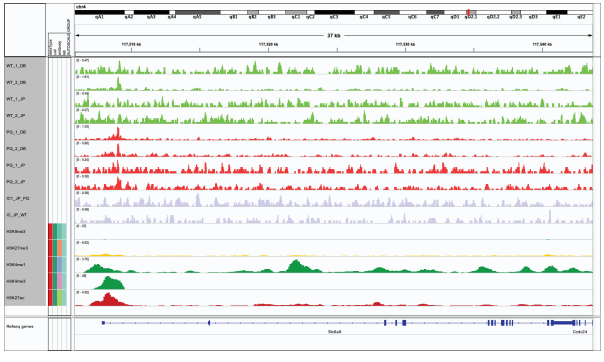
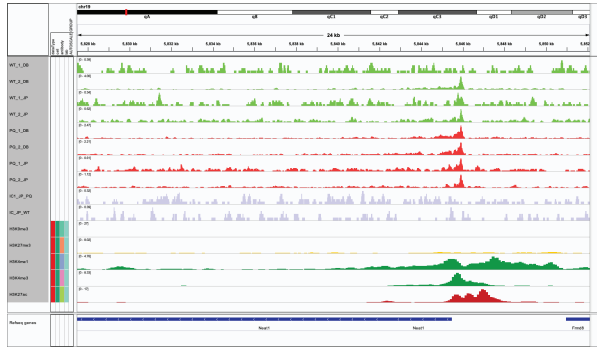
D *Neat1*